WFC3 UVIS PSF Evaluation in Thermal-Vacuum Test #1

G. F. Hartig
February 22, 2005

ABSTRACT

We have assessed the image quality of the WFC3 UVIS channel in a flight-like thermal-vacuum environment, but with its flight detector installed in a somewhat misaligned condition. Point source measurements at 16 field positions and four wavelengths indicate excellent imaging performance for the UVIS channel. Encircled energies readily meet expectations over the field, with CASTLE stimulus illumination. Models including the mid-frequency WFE of the HST OTA indicate that the on-orbit EE will likely meet the goal levels at 633 nm but fall just short of the core CEI specification at 250 nm, which is overly stringent.

Introduction

We have previously discussed measurements of the UVIS PSF at four field positions, through four filters spanning the spectral range, in ambient conditions in the SSDIF at GSFC (Hartig and Baggett, 2004a). The image quality was generally found to be excellent at these points near the center of each quadrant of the FOV. The PSF evaluation reported herein extends those results to full field coverage, with measurements made in a flight-like thermal-vacuum environment in the SES chamber at GSFC, using the CASTLE stimulus.

Although the flight UVIS CCD detector (UV-01) was found to be somewhat misaligned during ambient testing in early 2004, the WFC3 integration and test schedule required that the first instrument-level thermal vacuum test proceed without correction of the alignment error (Hartig, 2005). Modeling indicates that the impact on image quality is insignificant over most of the field, as long as the focus is optimally adjusted and stable. This will generally not be the case on-orbit, since the focus drifts with each orbit (thermal effects cause the OTA "breathing") as well as long-term (due to desorption of the OTA structure).

Procedure

After the instrument reached thermal equilibrium in the "hot operate" vacuum environment, the UVIS corrector was adjusted slightly in tip/tilt, as well as in focus, to optimize the image quality over the field. The resultant corrector mechanism settings, determined from analysis of alignment tests on 14 Sep 2004 to minimize coma and defocus over the 16 measured field points, are shown in Table 1. Although the PSF measurements were obtained about 2 weeks later, with the instrument in a "cold operate" environment, alignment measurements made at about the same time indicate no significant alignment change from the "hot operate" condition (Hartig, 2005).

**Table 1. UVIS Corrector Mechanism Settings**

Focus (LDVT)	2305
Inner Cylinder	10217
Outer Cylinder	53431

The PSF data were obtained on 1 Oct 2004 with SMS UV11S01A-04A (image rootnames IU11Anxx; IDL database entries 15859:16074 and 17003:17033; quicklook log ID 2004275a). To maximize efficiency, 200 px square subarrays, approximately centered on each of the PSFs, were used to obtain pairs of images, through each of four filters: F275W, F336W, F625W and F814W, along with bias frames. The CASTLE provided narrow-band point source illumination with a 5 um pinhole, D2 lamp, and double monochromator with 13 nm bandpass, for the UV observations at 250 and 350 nm, and lasers at 633 and 810 nm through single-mode fibers for the R and I band filter data. The detector was operated at the nominal –83C on-orbit temperature.

In addition to the subarray images, pairs of deep full frame images, with the image cores saturated by factors of ~5 and 50, were also obtained at one field point for each of the 4 wavelengths, to better assess the PSF far wings and search for straylight effects, such as the CCD scatter halo seen at long wavelengths in the STIS and ACS HRC detectors. Dark images, following highly saturated PSF images, were also obtained to evaluate image persistence effects in the CCDs. As in the previous ambient testing (Hartig and Baggett, 2004b), no significant image persistence was discovered.

Results

A montage of the images at each field point is displayed for each wavelength, with a log stretch over ~6.5 dex, in Figure 1. The diffraction-induced growth of the PSF with wavelength is apparent. Note the faint "donut" ghost images, with strong field dependence, produced by the F275W filter, even in narrow-band illumination well within the filter passband; these are discussed by Brown and Lupie (2004). The images at UVN14 suffer from a single blocked column, but its effect on the analysis is very minor. The images are clearly not centered on the field of view, and the pattern is rotated slightly CCW, due to misalignment of the detector (Hartig, 2005).
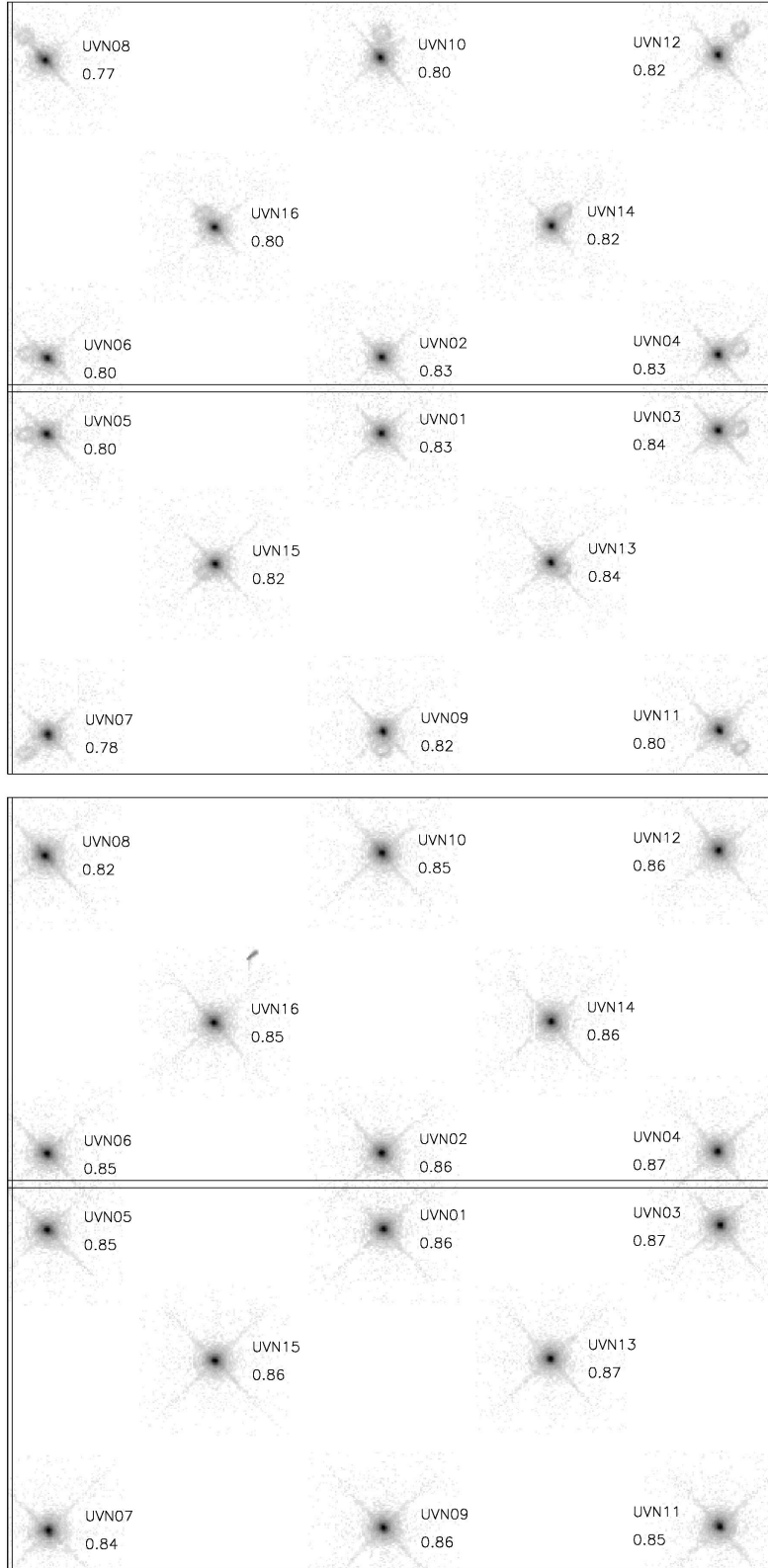
Figure 1. Montages of measured PSF images at 16 field points and at wavelengths 250 nm (top) and 350 nm (bottom). The images, shown centered at their actual locations in the field of view but with magnification of 8, have had background subtracted and first-order geometrical distortion removed. Measured encircled energy within diameters of 0.20 arcsec (250 nm) or 0.25 arcsec (all other wavelengths) are shown.
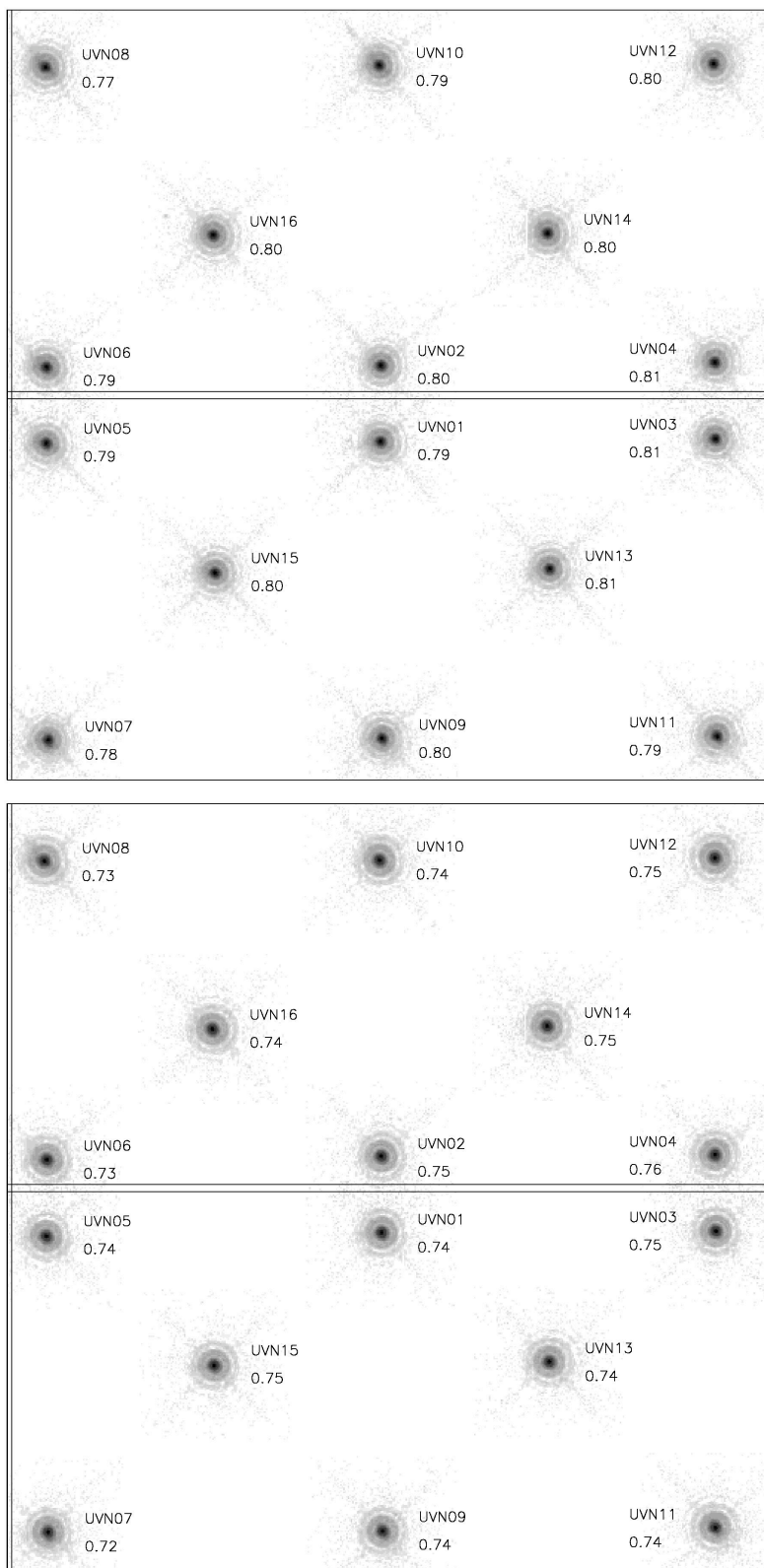
Figure 1 (cont'd). Montages of measured PSF images at 16 field points and at wavelengths 633nm (top) and 810 nm (bottom), indicating encircled energies within 0.25 arcsec diameter.

The encircled energy (EE) as function of radius from PSF center was computed for each of the unsaturated images, using IDL code previously developed and used for COSTAR, STIS and ACS alignment and verification. Briefly, the code corrects for first-order geometrical distortion, finds the image center at which the EE in a small diameter (0.15 arcsec) is maximized, computes the radius of each pixel from that center and, after subtracting a background that is adjusted so that the EE curve asymptotes to 1 with 0 gradient at a specified radius (2 arcsec for these subarray images), sums the normalized flux contribution within discrete radii, including estimation of partial pixel contributions. The results are presented in Table 2, and shown in Figure 1 for diameters of 0.2 arcsec (250 nm) or 0.25 arcsec (other wavelengths), for each of the measured field points. The peak pixel fraction (useful for exposure time estimation with regard to saturation avoidance) is also included in Table 2. Note that the peak fraction is highly sensitive to centration on the pixel grid, especially at short wavelengths where the Airy disk is undersampled. Previous modeling has shown that PSFs centered on the pixel corners can produce peak fraction ~5% (absolute) lower than those centered on a pixel, at 250 nm (Hartig and Baggett, 2004a).
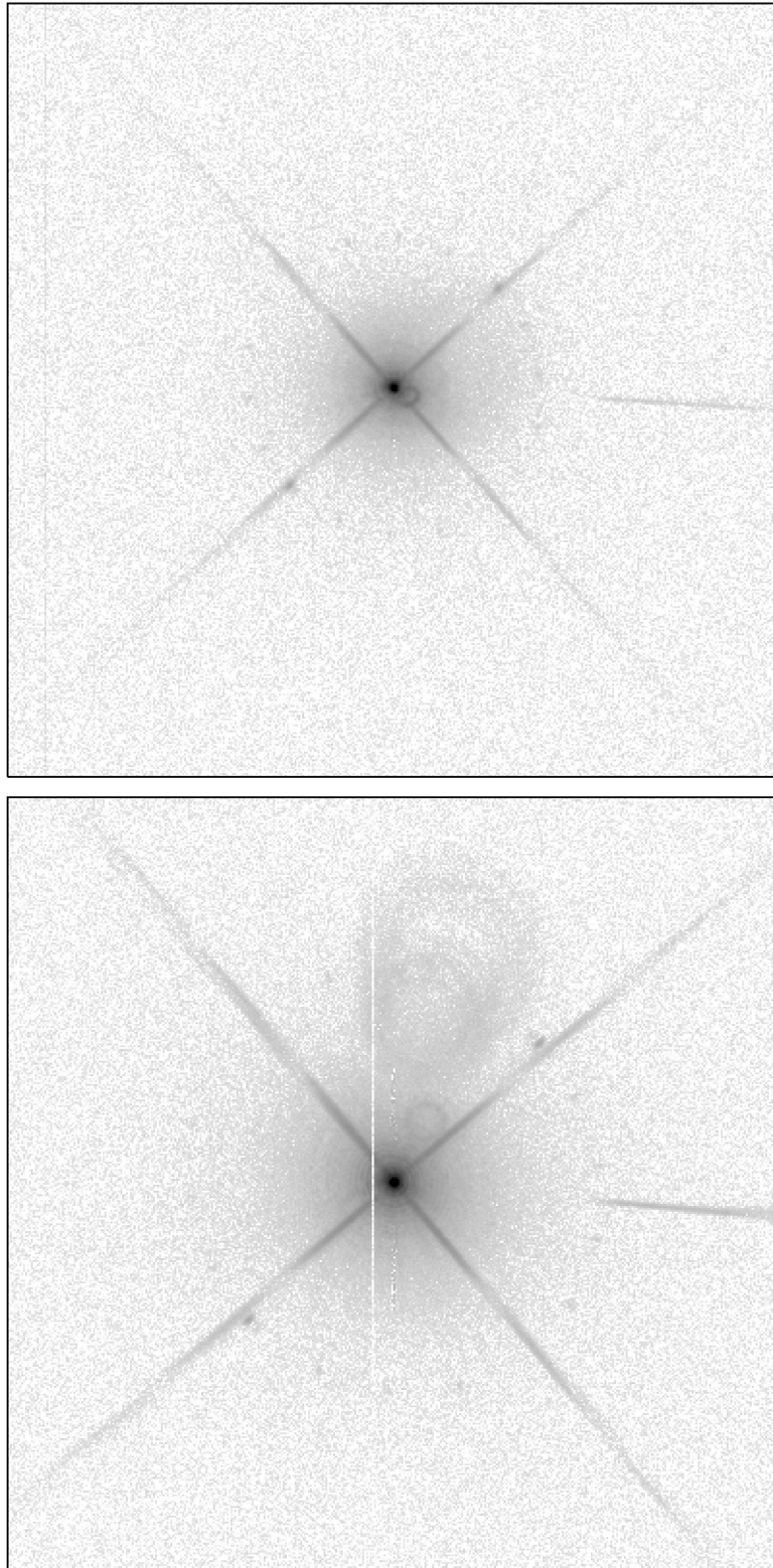
For a more extensive assessment of the PSF at the quadrant center field points, long-exposure, saturated images were combined with unsaturated ones to produce the high dynamic range images shown in Figure 2. The apparent peak pixel signal of each image is approximately 10^7 e$^-$, scaled by relative exposure time from the measured signal of ~50 ke$^-$. There are several interesting features present in the images, which subtend 16 arcsec square. The streaks at position angle ~266°, seen in the UVN13 and 14 (250 and 350 nm) images, are due to straylight reflections from a baffle in the CASTLE source assembly. There is a slightly "warm" column in the UVN13 image and a blocked column in the UVN14 image. Each of these was corrected by replacement with adjacent pixel averages before analysis.

Also apparent is a curious set of 18 faint spots arrayed in a ring centered on the UV point source images. The radius is proportional to the wavelength, indicating a diffraction phenomenon, and the position angle does not vary with field location, as do the spider diffraction features, which implicates a source on, or downstream of, the CASTLE steering flats, perhaps within the WFC3 instrument. This ring is at the same radius as the two brighter, diametrically opposed spots, just off the lower-left and upper-right (spacecraft V2 axis) spider features, that exhibit the same behavior. Their origin indeterminate, these features were left uncorrected.

Several ghost features are also present. The set of large diameter "donut" ghosts apparent in all but the 250 nm images are due to reflections between the four surfaces of the two detector windows, as expected. Smaller diameter ring ghosts closer to the PSF centers are due to the F275W and F336W filters; their integrated energy fractions are ~0.7% and ~0.03%, respectively. A faint, point-like ghost is also produced by the F625W filter, at PA~95° in the image at field point UVN15.

Table 2. Measured Encircled Energy and Peak Fraction

UVN01 λ (nm)	peak	0.15	0.2	0.25	0.35	UVN09 λ (nm)	peak	0.15	0.2	0.25	0.35
250	0.169	0.729	0.825	0.874	0.920	250	0.160	0.707	0.823	0.878	0.921
350	0.171	0.693	0.806	0.859	0.909	350	0.162	0.683	0.801	0.858	0.914
633	0.110	0.549	0.692	0.794	0.882	633	0.101	0.555	0.696	0.800	0.881
810	0.113	0.507	0.626	0.744	0.863	810	0.129	0.511	0.623	0.736	0.860
UVN02 λ (nm)	peak	0.15	0.2	0.25	0.35	**UVN10** λ (nm)	peak	0.15	0.2	0.25	0.35
250	0.180	0.727	0.826	0.874	0.920	250	0.164	0.698	0.797	0.850	0.904
350	0.150	0.685	0.805	0.860	0.911	350	0.137	0.672	0.791	0.846	0.900
633	0.130	0.550	0.702	0.801	0.889	633	0.116	0.545	0.686	0.788	0.872
810	0.110	0.513	0.634	0.747	0.868	810	0.112	0.507	0.625	0.741	0.863
UVN03 λ (nm)	peak	0.15	0.2	0.25	0.35	**UVN11** λ (nm)	peak	0.15	0.2	0.25	0.35
250	0.188	0.745	0.838	0.883	0.922	250	0.128	0.676	0.802	0.869	0.919
350	0.139	0.711	0.820	0.868	0.915	350	0.145	0.666	0.790	0.851	0.912
633	0.128	0.568	0.709	0.809	0.884	633	0.134	0.551	0.698	0.790	0.878
810	0.127	0.521	0.635	0.747	0.870	810	0.120	0.505	0.623	0.740	0.859
UVN04 λ (nm)	peak	0.15	0.2	0.25	0.35	**UVN12** λ (nm)	peak	0.15	0.2	0.25	0.35
250	0.163	0.728	0.830	0.879	0.921	250	0.173	0.720	0.820	0.871	0.918
350	0.136	0.703	0.817	0.869	0.918	350	0.172	0.699	0.807	0.857	0.910
633	0.119	0.561	0.702	0.809	0.888	633	0.103	0.555	0.697	0.803	0.879
810	0.109	0.514	0.635	0.756	0.872	810	0.109	0.512	0.631	0.751	0.870
UVN05 λ (nm)	peak	0.15	0.2	0.25	0.35	**UVN13** λ (nm)	peak	0.15	0.2	0.25	0.35
250	0.145	0.685	0.799	0.858	0.912	250	0.203	0.747	0.837	0.884	0.922
350	0.137	0.673	0.793	0.850	0.909	350	0.161	0.711	0.822	0.872	0.918
633	0.121	0.546	0.690	0.791	0.877	633	0.119	0.568	0.708	0.809	0.883
810	0.109	0.503	0.624	0.738	0.861	810	0.129	0.522	0.635	0.745	0.869
UVN06 λ (nm)	peak	0.15	0.2	0.25	0.35	**UVN14** λ (nm)	peak	0.15	0.2	0.25	0.35
250	0.165	0.688	0.796	0.853	0.908	250	0.184	0.729	0.824	0.871	0.917
350	0.140	0.672	0.790	0.846	0.903	350	0.159	0.697	0.811	0.863	0.911
633	0.132	0.546	0.690	0.788	0.873	633	0.135	0.557	0.704	0.803	0.883
810	0.118	0.506	0.621	0.735	0.861	810	0.118	0.514	0.630	0.746	0.869
UVN07 λ (nm)	peak	0.15	0.2	0.25	0.35	**UVN15** λ (nm)	peak	0.15	0.2	0.25	0.35
250	0.113	0.638	0.782	0.855	0.916	250	0.150	0.712	0.821	0.875	0.921
350	0.127	0.631	0.768	0.843	0.913	350	0.160	0.686	0.804	0.861	0.914
633	0.108	0.530	0.675	0.779	0.874	633	0.128	0.556	0.698	0.802	0.889
810	0.114	0.493	0.606	0.718	0.850	810	0.096	0.505	0.632	0.749	0.868
UVN08 λ (nm)	peak	0.15	0.2	0.25	0.35	**UVN16** λ (nm)	peak	0.15	0.2	0.25	0.35
250	0.145	0.662	0.770	0.832	0.896	250	0.178	0.701	0.804	0.859	0.911
350	0.131	0.646	0.763	0.825	0.888	350	0.139	0.677	0.795	0.852	0.907
633	0.103	0.528	0.669	0.773	0.861	633	0.110	0.553	0.696	0.799	0.883
810	0.110	0.500	0.608	0.731	0.854	810	0.106	0.508	0.624	0.740	0.862

Figure 2. High dynamic range composite images at 250 nm (top, at UVN13) and 350 nm (bottom, at UVN14) shown on a log stretch from 1 to 10^6 e⁻, covering 16 arcsec square. Flares at PA ~266 are due to a CASTLE straylight reflection.
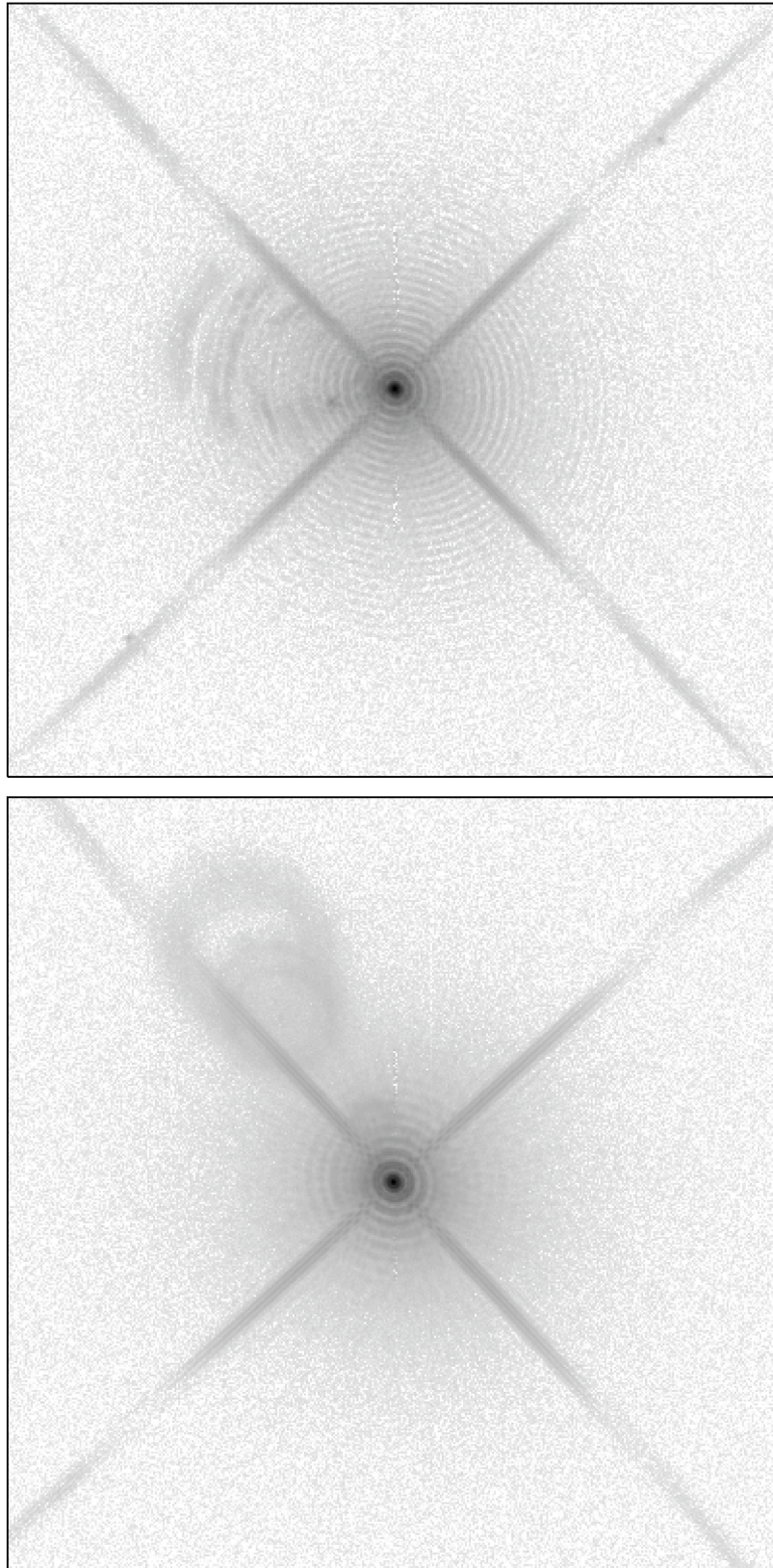
Figure 2 (cont'd.) High dynamic range composite images at 633 nm (top, at UVN15) and 810 nm (bottom, at UVN16) shown on a log stretch from 1 to 10^7 e⁻, covering 16 arcsec square.

In an earlier study of the UVIS PSFs (Hartig and Baggett, 2004a), straightforward modeling, including only an independent assessment of the low order WFE, the pupil mask and a reasonable estimate of the detector MTF, yielded good agreement with the measured EE curves at 350 and 633 nm. Applying the same models to the current set of measurements also results in good agreement, but the match is improved with use of somewhat smaller detector MTF effects. A credible explanation for the improvement is the lack of image smearing in the current thermal-vacuum data due to turbulence present in the ambient images. The best empirical fit to the pixel response convolution kernel is shown in Table 3. These results indicate that the CEI specification requiring that 90% of the energy from a small spot lie within the central pixel is not met.

Table 3. CCD Pixel Response Functions

| 250 nm			810 nm		
0.027	0.111	0.027	0.002	0.037	0.002
0.111	0.432	0.111	0.037	0.844	0.037
0.027	0.111	0.027	0.002	0.037	0.002

After making very minor corrections in the composite images for the bad columns, and the CASTLE "streaks", we have computed the EE and azimuthally-averaged (AA) PSF, normalized to 1 at the peak, for comparison with model and specifications. These are shown in Figure 3, which plots the measured EE (left panel) and AA PSF intensity (right panel) as solid lines, with the CASTLE+WFC3 model shown as dotted lines. The agreement between measurement and model is very good, from radii of 40 mas (1px) to 5 arcsec. The differences in modulation of the AA PSF wings beyond 1 arcsec are at least partially due to inaccuracies in the model related to the diffraction of the spiders.

Because the EE specification applies to the WFC3 installed in the HST, the ground-based measurements must be extrapolated with the aid of model computations that account for differences between the CASTLE and HST to predict on-orbit performance. These differences and the limitations of the modeling are described in Hartig and Baggett (2004a). The EE specifications in the PSF wings (for 250 nm and 633 nm) are shown in Figure 3 as diamonds. If taken at face value, the plots indicate that the camera readily meets its requirements. Actual on-orbit performance, including the HST telescope properties, is approximated by the dashed OTA+WFC3 model curves, which show the effects on the near wings of the OTA mid-frequency WFE. While the projected EE at 633 nm (83% in 0.25 arcsec) exceeds the specified goal, the 250 nm EE in 0.2 arcsec diameter is expected to fall just below the requirement (75%), which was overly stringent, given the known OTA performance. This shortfall is not indicative of lack of optical performance of the WFC3 UVIS channel.
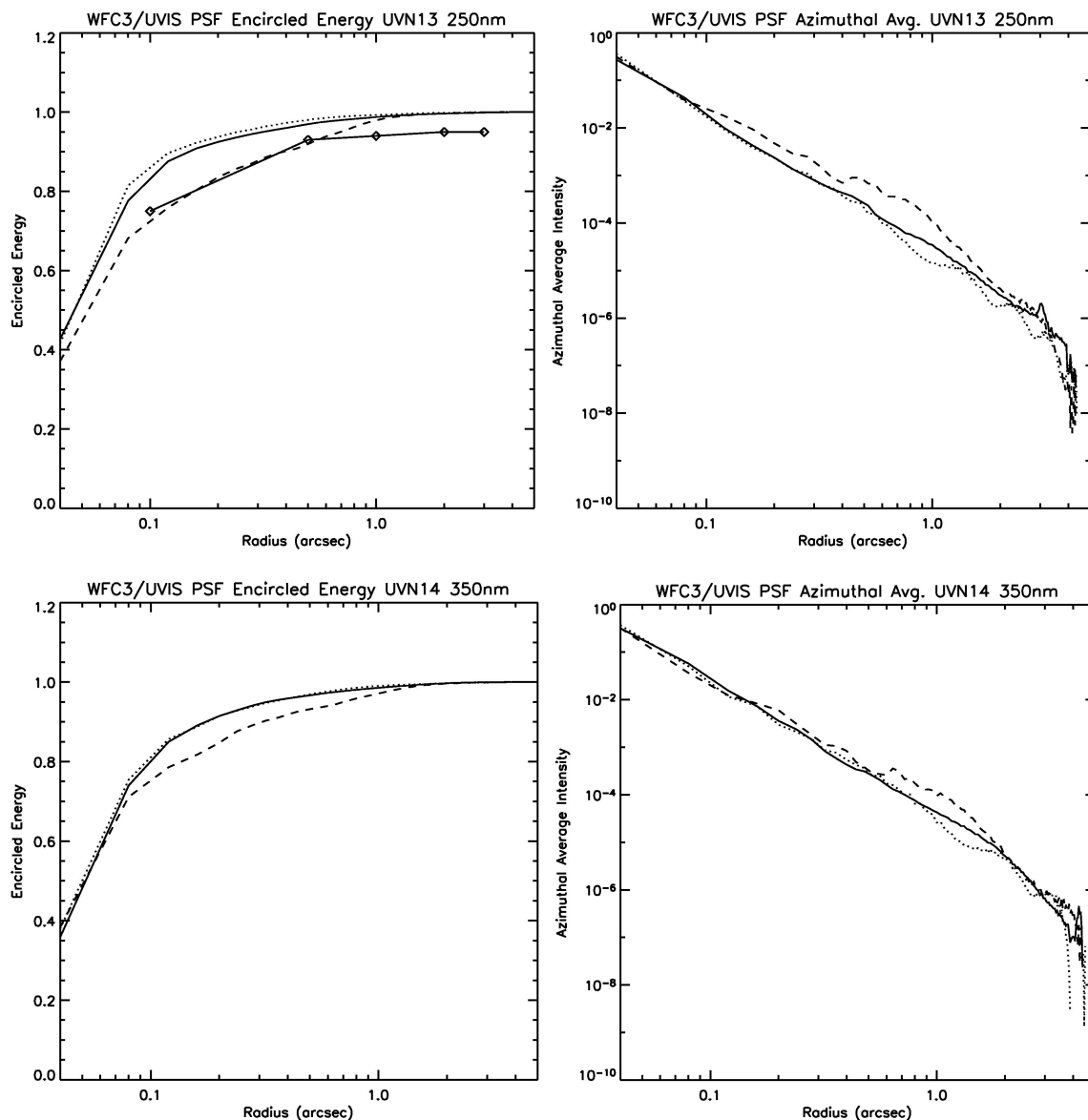
Figure 3. Comparison of composite measured (solid line), CASTLE model (dotted line), and OTA model (dashed line) images at field points UVN13 and UVN14 at 250, and 350 nm, respectively. The left frames show the encircled energy, from radii of 1 px to 5 arcsec, and the right frames plot the azimuthally-averaged PSF. The EE specifications (at 250 nm) are shown as diamonds.
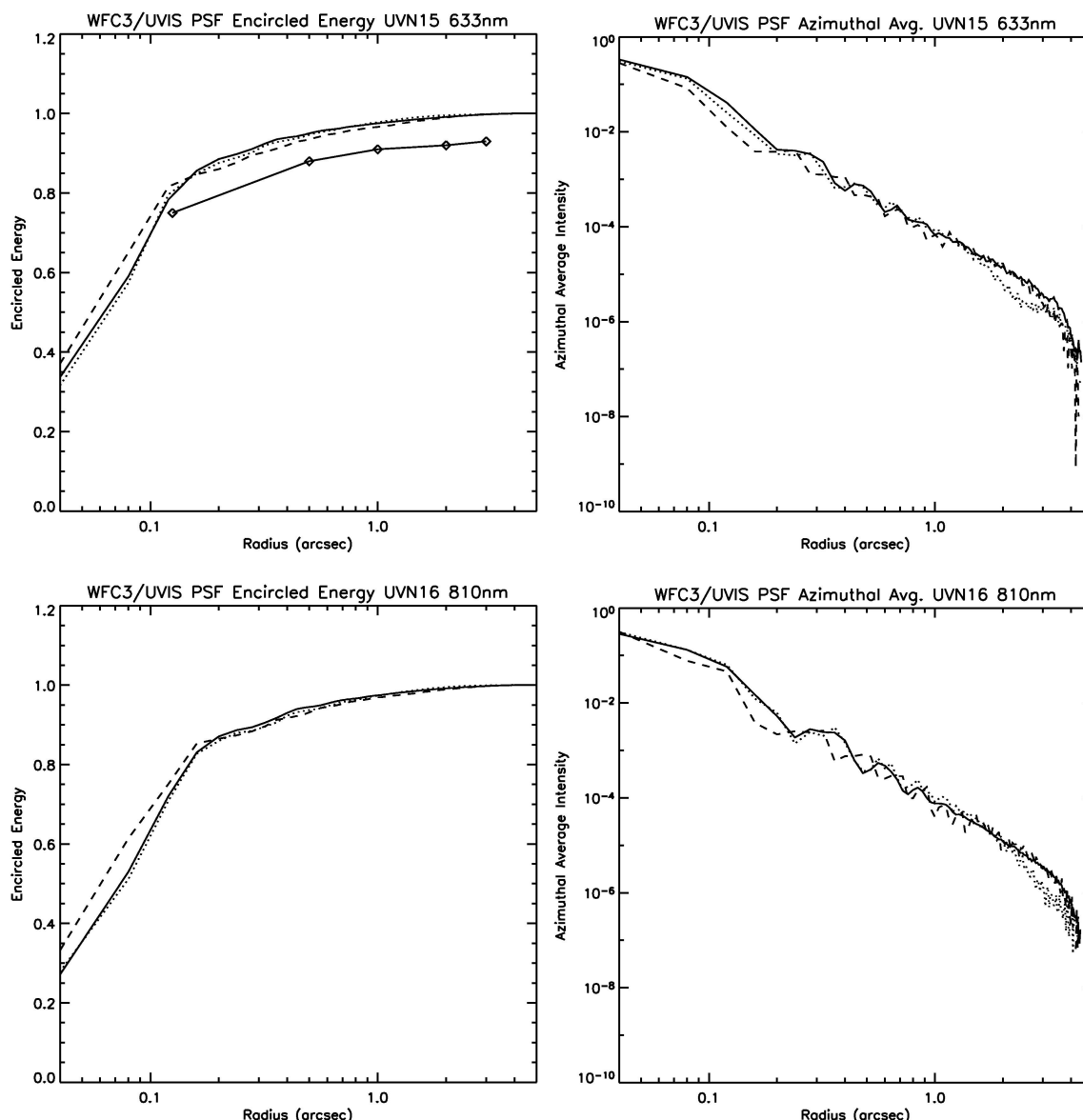
Figure 3 (cont'd.) Comparison of composite measured (solid line), CASTLE model (dotted line), and OTA model (dashed line) images at field points UVN15 and UVN16 at 633 and 810 nm, respectively. The left frames show the encircled energy, from radii of 1 px to 5 arcsec, and the right frames plot the azimuthally-averaged PSF. The EE specifications (at 633 nm) are shown as diamonds.

Conclusion

We conclude that the WFC3 UVIS optical performance is generally excellent. Aside from the anomalous filter ghosts, such as those readily apparent in the F275W images (see Brown and Lupie, 2004, for a complete discussion) and a very faint enigmatic ring of spots and an accompanying symmetrical pair of weak straylight features the origin of which is not yet understood, the UVIS channel is performing as expected over the field. With proper alignment of the detector, notably in its tilt about the X axis, the performance should improve slightly at the field edges from the levels demonstrated here.

Our modeling indicates that the UVIS channel will readily meet its on-orbit image quality (EE) specifications at 633 nm, but that the requirements at 250 nm will likely not be achieved, through no fault of the WFC3, due to the mid-frequency WFE of the HST OTA. A waiver or amendment of the 250 nm EE requirements is in order. The CCD pixel response function specification will also not be met at any wavelength.

References

Brown, T. and Lupie, O. "Filter Ghosts in the WFC3 UVIS Channel", STScI ISR WFC3-2004-04, 2004.

Hartig, G.F. and Baggett, S. "Preliminary WFC3 UVIS PSF Evaluation", STScI ISR WFC3-2004-08, 2004a.

Hartig, G.F. and Baggett, S. "Preliminary Assessment of Image Persistence in the WFC3 UVIS CCD Detector", STScI ISR WFC3-2004-09, 2004b.

Hartig, G.F. "WFC3 Flight Detector Alignment Characterization in Thermal-Vacuum Test #1", STScI ISR WFC3-2005-04, 2005.